Shot-profile true amplitude cross-correlation imaging condition

B. Arntsen[1], *A. Kritski*[2], *B. Ursin*[1] *and L. Amundsen*[2]

ABSTRACT

The U/D imaging condition for shot profile migration can be used to estimate the angle dependent reflection coefficient, but is difficult to implement numerically because of the spectral division involved. Most techniques for stabilizing the division requires a damping factor which might be difficult to estimate and which also introduces bias into the final result. A stable result can be achieved by approximating the imaging condition with a cross-correlation of the up- and downgoing wavefields at zero time lag, but this will lead to incorrect Amplitude-Versus-Angle (AVA) behavior of the estimated reflection coefficient. We use a simple model for wavepropagation of primary reflections in the wave-number frequency domain and invert the model with respect to the reflection coefficient. By using the properties of wavefield extrapolators it can then be shown that the reflection coefficients can be estimated by cross-correlation of the upgoing wavefield and a downgoing wavefield where the initial wavefield is the inverse of the wavefield generated by a point source. The new imaging condition gives the correct Angle-versus-Amplitude behavior for horizontal reflectors. For dipping reflectors it is shown that a post-migration correction factor can be used to recover the correct angle behavior of the reflection coefficient. The new imaging condition is numerically stable, does not involve damping factors, is simple to implement numerically and is a simple modification of the classical cross-correlation imaging condition. Numerical examples confirm the correct AVA behavior of the new imaging condition.

INTRODUCTION

Depth imaging should ideally be capable of recovering not only an image of the subsurface, but also angle dependent reflection coefficients. For depth migration schemes based on high-frequency asymptotics there are established and well developed amplitude preserving algorithms (Bleistein, 1987; Tygel et al., 1993; Schleicher et al., 1993; Ursin, 2004) capable of computing estimates of angle dependent reflection coefficients in addition to structural images.

For migration based on one-way wave equations Claerbout (1971) introduced an imaging condition for shot-profile migration using the ratio between up- and downgoing wavefields giving correct estimates of the reflection coefficient (Deng and McMechan, 2007). However this condition is difficult to implement due to the instability of spectral division leading to increased noise level. A wide variety of approaches to stabilize Claerbout (1971)'s imaging

[1]Norwegian University of Science and Technology (NTNU, Department of Petroleum Engineering & Applied Geophysics, E-mail: borge.arntsen@ntnu.no
[2]Statoili Research Centre

condition have been investigated by Cazzola et al. (2002); Valenciano and Biondi (2003); Zhang et al. (2005); Ursin et al. (2012) and Schleicher et al. (2008).

Claerbout (1971) also suggested an approximate cross-correlation imaging condition for shot-profile migration which has been extensively used due to its simplicity and stability. Rickett and Sava (2002) extended this imaging condition to include offset information and to compute angle gathers. Designed for structural imaging this approach do not give correct estimates of the Amplitude-Versus-Angle (AVA) response.

We derive a modification of Claerbouts cross-correlation imaging condition which produces common-angle gathers with correct amplitude-versus-angle relationship or conventional stacks with better estimates for the angle-averaged reflectivity. The method is simple to implement and requires only a modification of the initial wavefield in the downward propagation and decomposition into plane-waves in the midpoint-slowness domain (de Bruin et al., 1990). The method estimates amplitude-versus-angle responses from both locally plane and dipping reflectors, given that the local dip-angle is known.

In the next section we consider a simple model for primary reflections and derive the new imaging condition by inverting the model with respect to the reflection coefficient. We also compare our method with other approaches to shot-profile migration. The section on numerical results demonstrate that correct AVA-response can be obtained both for simple models and a more realistic reservoir model.

IMAGING CONDITION

We consider a single shot record with a seismic source at lateral position $\boldsymbol{x}_s$ at the surface of an acoustic medium where the wave propagation velocity, c, and density, ρ, are functions of depth only. We consider plane waves where the principal direction of propagation is taken along the x_3 axis ("depth") and the transverse axes are (x_1, x_2). The wavenumber is denoted by $\boldsymbol{k} = (k_1, k_2, k_3)$ The wavenumber $\boldsymbol{k}$ is related to the slowness $\boldsymbol{p}$ by

$$\boldsymbol{k} = \omega \boldsymbol{p}, \tag{1}$$

where ω is the angular frequency and the vertical wavenumber k_3 is given by

$$k_3 = \begin{cases} \sqrt{(\omega/c)^2 - k_1^2 - k_2^2} & ,\text{if } \sqrt{k_1^2 + k_2^2} \leq \omega/c, \\ i\sqrt{k_1^2 + k_2^2 - (\omega/c)^2} & ,\text{if } \sqrt{k_1^2 + k_2^2} > \omega/c. \end{cases} \tag{2}$$

Pressure normalized imaging condition

Decomposition into down and upgoing wavefields is not unique and depends on the scaling of the eigenvectors (Ursin, 1983; Ursin et al., 2012). The most common approach is to use so-called pressure normalization, where the upgoing wave U at depth x_3 can be related to the downgoing wavefield D at the same depth using a simplified model for primary reflections, as shown in equation (A-18) in the appendix

$$U(x_3) = R(x_3)D(x_3). \tag{3}$$

Here R is the reflection coefficient, and the downgoing wavefield D at depth can be estimated from the downgoing wavefield at the surface D_0 by

$$D(x_3) = \exp\left[\int_0^{x_3} ik_3(\zeta)d\zeta\right] D_0, \tag{4}$$

where D_0 is due to a point source

$$D_0 = -\frac{2\pi S(\omega)\exp(-i\boldsymbol{q}\cdot\boldsymbol{x}_s)}{ik_3}. \tag{5}$$

Here $S(\omega)$ is the source signature, $\boldsymbol{q} = (k_1, k_2)$ is the transverse wavenumber while $\boldsymbol{x}_s = (x_{s1}, x_{s2})$ is the source position. The upgoing wavefield is computed from the data U_0 at the surface

$$U(x_3) = \exp\left[-\int_0^{x_3} ik_3(\zeta)d\zeta\right] U_0. \tag{6}$$

The reflection coefficient can be found from equation (3) as

$$R(x_3) = \frac{U(x_3)}{D(x_3)}, \tag{7}$$

and by using equations (4) and (5), equation (7) becomes

$$R(x_3) = U(x_3)D'^*(x_3), \tag{8}$$

where the new downgoing wavefield D'

$$D'(x_3) = \exp(ik_3x_3)D'_0, \tag{9}$$

is due to an initial inverse downgoing wavefield

$$D'_0 = \exp(-i\boldsymbol{q}\cdot\boldsymbol{x}_s)\frac{ik_3}{2\pi S^*(\omega)}. \tag{10}$$

The reflection coefficient in (8) can be Fourier-transformed over the wavenumbers and frequency to the spatial and time domain. Evaluating the reflection operator at time equal to zero, one obtains after converting integrals to sums

$$R(\boldsymbol{x}_m, \boldsymbol{h}, x_3) = \frac{1}{(2\pi)}\sum_{\omega}\sum_{\boldsymbol{x}_s} U(\boldsymbol{x}_m + \boldsymbol{h}/2, x_3, \boldsymbol{x}_s)D'^*(\boldsymbol{x}_m - \boldsymbol{h}/2, x_3, \boldsymbol{x}_s), \tag{11}$$

where the subsurface midpoint coordinates $\boldsymbol{x}_m = (\boldsymbol{x}_{m1}, \boldsymbol{x}_{m2})$ and offset coordinates $\boldsymbol{h} = (h_1, h_2)$ have been introduced and we have also introduced the dependency on the source coordinate $\boldsymbol{x}_s$. Note that the sum over the source coordinate $\boldsymbol{x}_s$ follows from the application of the Fourier transform and is not introduced ad hoc.

de Bruin et al. (1990) pointed out that the integration over frequency in equation (11) implies summation over plane waves with different angles. To ensure averaging the reflection operator over constant angles de Bruin et al. (1990) introduced a mapping to slowness

before summation. Following de Bruin et al. (1990) we then get the wave equation slowness transform:

$$R_s(\boldsymbol{x}_m, \boldsymbol{p}_h, z, \boldsymbol{x}_s) = \frac{1}{(2\pi)} \sum_{\omega} \sum_{\boldsymbol{h}} \exp(i\omega \boldsymbol{p}_h \boldsymbol{h}) U(\omega, \boldsymbol{x}_m - \boldsymbol{h}/2, z, \boldsymbol{x}_s) D'^{*}(\omega, \boldsymbol{x}_m + \boldsymbol{h}/2, z, \boldsymbol{x}_s), \tag{12}$$

where the slowness $\boldsymbol{p}_h$ is related to the offset wavenumber $\boldsymbol{k}_h$ by $\boldsymbol{p}_h = \boldsymbol{k}_h/\omega$. Summation over source positions improves the estimate and ensures proper angle coverage

$$R(\boldsymbol{x}_m, \boldsymbol{p}_h, z) = \sum_{\boldsymbol{x}_s} R_s(\boldsymbol{x}_m, \boldsymbol{p}_h, z, \boldsymbol{x}_s). \tag{13}$$

Equation (13) and (12) provide a new imaging condition which recovers correctly the angle-dependent plane-wave reflection coefficient given that the amplitudes of the up- and downgoing wavefields U and D are accurate. It avoids the division by the energy of the downgoing wavefield (Ursin et al., 2012) and gives a stable estimate of the plane-wave reflection coefficient.

Flux normalized imaging condition

By using flux-normalized wavefields the differential equations for the up- and downgoing waves becomes simpler and potentially will lead to more accurate wavefield extrapolation.

The flux normalized wavefields $\tilde{U}$ and $\tilde{D}$ are related through the equation (see equation (A-26) in the appendix)

$$\tilde{U}(x_3) = \tilde{R}(x_3)\tilde{D}(x_3), \tag{14}$$

where $\tilde{R}$ is given by equation (A-25).

The upgoing wavefield $\tilde{U_0}$ at the surface is related to the pressure-normalized field U_0 by (Ursin et al., 2012)

$$\tilde{U_0} = \sqrt{\frac{2}{Z}} U_0, \tag{15}$$

where the impedance Z is given by $Z = \rho\omega/k_3$. The initial inverse downgoing wavefield D' is obtained as (Ursin et al., 2012)

$$\tilde{D}'_0 = -\frac{\sqrt{\frac{1}{2}k_3\rho_0\omega}}{2\pi S^*(\omega)}. \tag{16}$$

Using the new flux-normalized wavefields $\tilde{U_0}$ and $\tilde{D}'_0$ wave extrapolation can be performed as for the downgoing wavefield as in equation (4) and (6). This estimate of the plane-wave reflection coefficient is computed from

$$\tilde{R}(\boldsymbol{x}_m, \boldsymbol{p}_h, z, \boldsymbol{x}_s) = \frac{1}{(2\pi)} \sum_{\omega} \sum_{\boldsymbol{x}_s} \sum_{\boldsymbol{h}} \exp(i\omega \boldsymbol{p}_h \boldsymbol{h}) \tilde{U}(\omega, \boldsymbol{x}_m - \boldsymbol{h}/2, z, \boldsymbol{x}_s) \tilde{D}'^{*}(\omega, \boldsymbol{x}_m + \boldsymbol{h}/2, z, \boldsymbol{x}_s). \tag{17}$$

Heterogeneous medium

The imaging conditions given above in equations (17) and (12) can be proved to be correct for heterogeneous media with smooth velocity variations. The up- and downgoing pressure normalized wavefields can then be recursively extrapolated using the explicit operator approach (Holberg, 1988)

$$\begin{aligned} U(x_1, x_2, x_3 + \Delta x_3) &= \sum_{x_1', x_2'} h^*(x_1 - x_1', x_2 - x_2', \omega/c) U(x_1', x_2', x_3), \\ D(x_1, x_2, x_3 + \Delta x_3) &= \sum_{x_1', x_2'} h(x_1 - x_1', x_2 - x_2', \omega/c) D(x_1', x_2', x_3), \end{aligned} \tag{18}$$

where h is a band-limited approximation to the phase-shift operator depending on the ratio between the frequency and the local velocity. Δx_3 is the discretization interval in the vertical direction. Equation (18) can also be used to extrapolate the flux-normalized wavefields $\tilde{U}$ and $\tilde{D}$.

RELATION TO OTHER IMAGING CONDITIONS

Rickett and Sava (2002) proposed the extended imaging condition given by:

$$R(\boldsymbol{x}_m, \boldsymbol{h}, z) = \frac{1}{2\pi} \sum_{\boldsymbol{x}_s} \sum_{\omega} U(\boldsymbol{x}_m - \boldsymbol{h}/2, z, \boldsymbol{x}_s) D^*(\boldsymbol{x}_m + \boldsymbol{h}/2, z, \boldsymbol{x}_s). \tag{19}$$

The imaging condition in equation (19) is similar to the imaging condition in equation (11), the only difference is that D' is substituted with D.

In the wavenumber-frequency domain the estimate $\hat{R}$ of the reflection coefficient corresponding to the extended imaging condition (Rickett and Sava, 2002) is equal to:

$$\begin{aligned} \hat{R}(x_3) &= R(x_3) D_0 {D_0}^* \\ &= R(x_3) \frac{|S(\omega)|^2}{4k_z^2}. \end{aligned} \tag{20}$$

Zhang and Sun (2008) proposed an imaging condition where the initial downgoing wavefield is given by

$$\hat{D}_0 = -\frac{\exp(-i\boldsymbol{q}_s \boldsymbol{x}_s) S(\omega)}{i\omega}, \tag{21}$$

which leads to the estimate of the reflection coefficient

$$\hat{R}(x_3) = R(x_3) \frac{|S(\omega)|^2}{2k_z \omega}. \tag{22}$$

Since k_z is proportional to $(\omega/c)\cos(\phi)$, where ϕ is the reflection angle, it is seen that the imaging condition given by equation (20) gives an estimate of the reflection coefficient proportional to the inverse of $\cos^2(\phi)$, whereas the estimate obtained from equation (22) is proportional to the inverse of $\cos(\phi)$.

AMPLITUDE VERSUS ANGLE (AVA) GATHERS

In the preceding sections we derived expressions for computing the reflection operator as a function of horizontal slowness, $\boldsymbol{p}_h$. For a wave reflected from a plane dipping reflector and where the velocity can be assumed to be constant equal to c, the relation between the incidence angle ϕ and slowness $\boldsymbol{p}_h$ is given by

$$\begin{aligned} p_{hx} &= \frac{1}{c}\sin(\phi)\cos(\alpha)\cos(\theta), \\ p_{hy} &= \frac{1}{c}\sin(\phi)\cos(\alpha)\sin(\theta), \end{aligned} \tag{23}$$

where ϕ is the reflection angle, α is the dip angle and θ is the direction of the maximum down-dip direction. Equation (23) can be used to map the reflectivity from offset slowness to opening- and dip-angle.

In Appendix B it is shown that the reflection coefficient for a dipping plane reflector for the pressure-normalized case is given by

$$R(\phi,\alpha,z) = \left[\frac{2\cos(\phi-\alpha)}{\cos(\phi+\alpha)+\cos(\phi-\alpha)}\right] r(\phi-\alpha), \tag{24}$$

where r is the linearized plane wave reflection coefficient. If we assume that the wave velocities in the neighborhood of a given midpoint location are approximately constant, we can use equation (24) to compute the plane wave reflection coefficient from the reflection operator as:

$$r(\phi-\alpha) = R(\phi,\alpha,z)\left[\frac{\cos(\phi-\alpha)+\cos(\phi+\alpha)}{2\cos(\phi-\alpha)}\right]. \tag{25}$$

For the flux-normalized approach one gets

$$r(\phi-\alpha) = \tilde{R}(\phi,\alpha,z)\left[\frac{\cos(\phi-\alpha)+\cos(\phi+\alpha)}{2\sqrt{\cos(\phi+\alpha)\cos(\phi-\alpha)}}\right]. \tag{26}$$

The above relations show that to successfully extract the plane-wave reflection coefficient from the reflection operator, the local reflector dip must be known. An advantage of equations (25) and (26) is that the computation of reflection coefficients can be performed post-migration.

In the next section we demonstrate the use of the new imaging condition given by equation (13) using both simple acoustic models and a more realistic elastic reservoir model.

NUMERICAL RESULTS

In the examples below the reflection operator is computed using equations (13) and (12), while the plane wave reflection coefficient is extracted using equation (25). The initial inverse wavefield D_0' is computed in the wave-number frequency domain by equation (6).

Layer Thickness (m)	Velocity (m/s)	Density (kg/m^3)
1000	2000	1000
1000	2000	1200
1000	2000	1000
-	2000	1200

Table 1: Horizontally layered model, with density contrast between layers. The velocity is constant for all layers.

Acoustic models

The model shown in table 1 consists of four plane layers where the density is different in each layer, while the velocity is kept constant throughout the model at 2000 m/s. Synthetic shot records were generated using the model given in table 1 by a finite-difference acoustic modeling program. A split-spread acquisition geometry was used with 10 meter receiver distance and a maximum half-offset of 5 km and a shot spacing of 10 meters. The source signature was a Ricker wavelet with a peak frequency of 20 Hz. A single shot record is shown in Figure 1 . Equation (13) and equation (25) were used to compute the angle

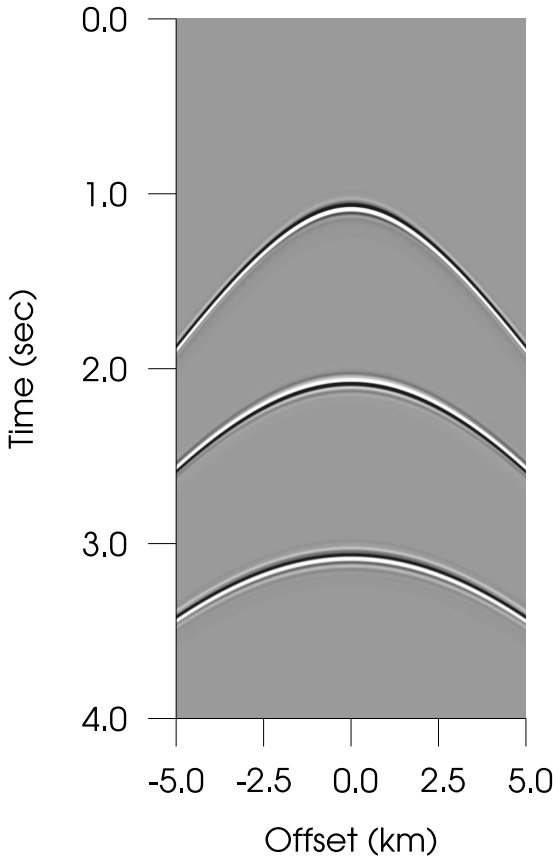

Figure 1: Shot record generated using the layered model given in table 1

gather shown in Figure 2. The right hand part of Figure 2 shows RMS amplitude picks extracted along the three events in the angle gather. A common scale factor before plotting

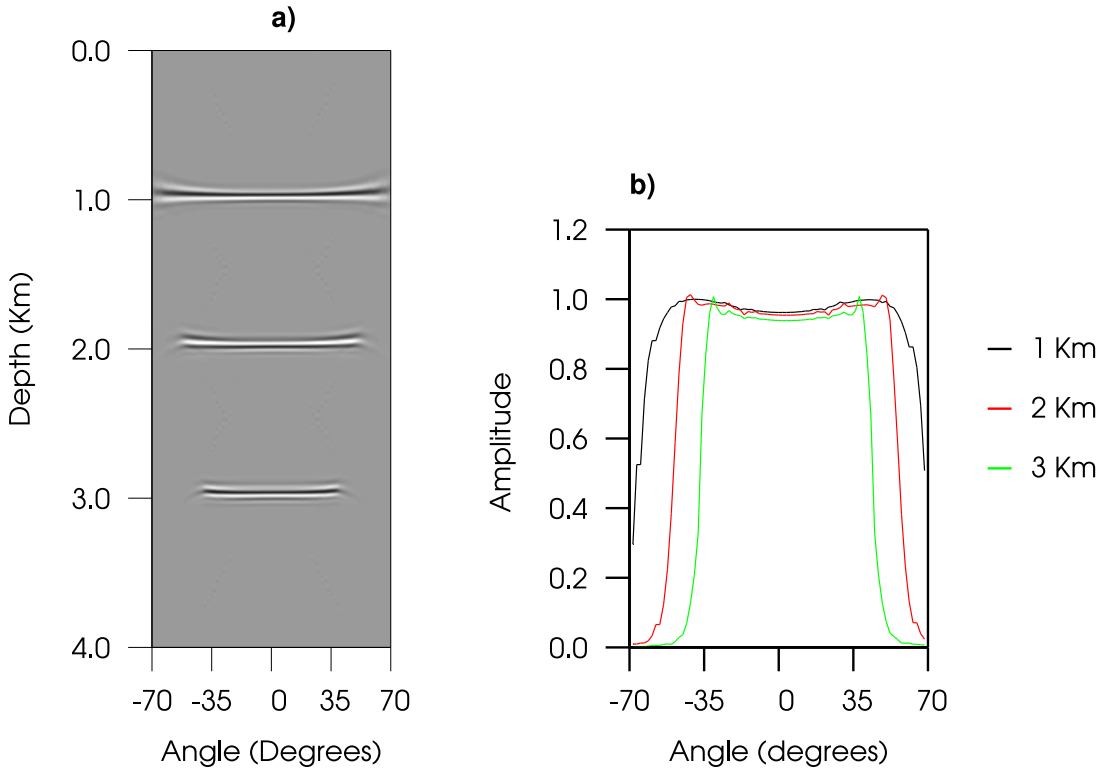

Figure 2: a) Angle gather for the plane layered model given in table 1 and b) RMS amplitude picks of the angle gathers. The amplitude versus angle is seen to be constant, which is consistent with a model with density contrasts only.

was applied to the three amplitude curves, such that the largest amplitude for the reflector at 1 km depth (black curve) is equal to one. The relative amplitudes between the reflectors are thus preserved. The amplitude versus angle shows no significant angle dependence, as is expected in the case of reflectors with pure density contrast. Moreover the amplitude levels of the three events are also approximately equal.

Table 2 contains a plane layered model with velocity contrasts, and a corresponding shot record was computed as in the first example. An angle gather was computed in a similar

Layer Thickness (m)	Velocity (m/s)	Density (kg/m^3)
1000	2000	1000
1000	2200	1000
1000	2000	1000
-	2200	1000

Table 2: Horizontally layered model, with velocity contrast between layers. The density is constant for all layers.

way as for Figure 2 and shown in Figure 3 together with the RMS amplitude picks for the

events at a depth of 2 and 3 km. The black solid line shows the theoretical amplitude versus

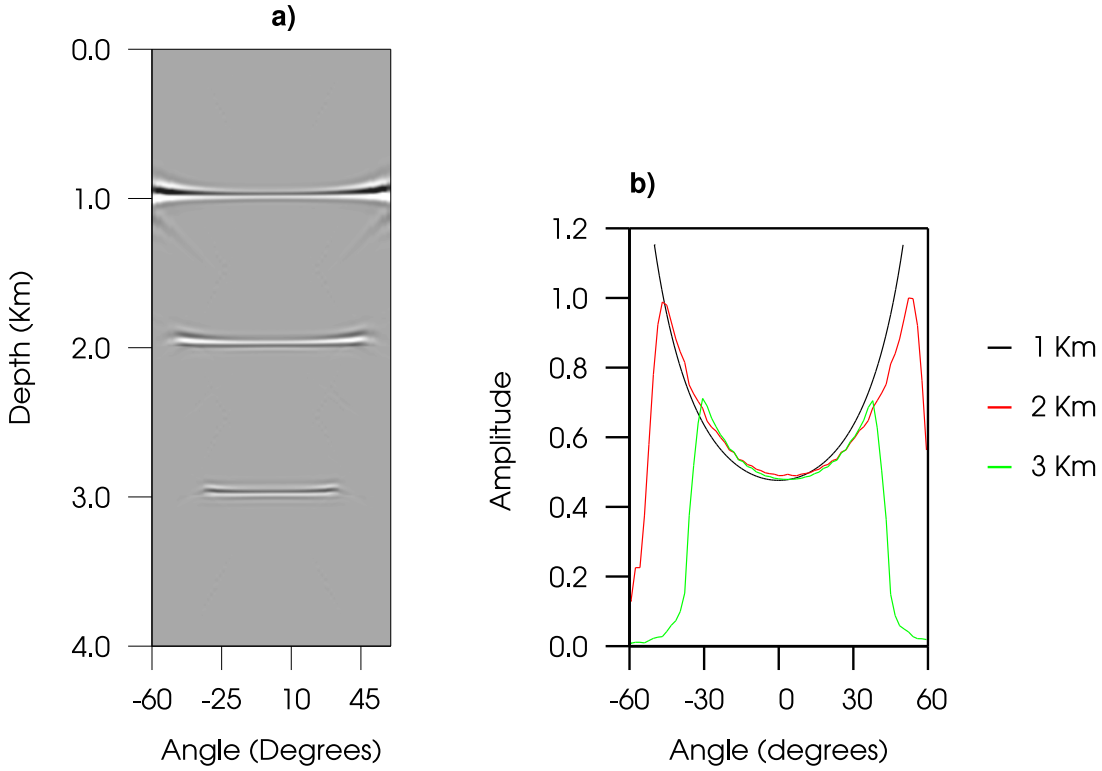

Figure 3: Angle gather for the plane layered model given in table 2 and b) RMS amplitude picks of the events at depths 2 and 3 km. The black solid line is the theoretical amplitude versus angle response.

angle response, which seems to fit well with the amplitudes picked from the angle gather.

In Figure 4 we have used the extended imaging condition given by Rickett and Sava (2002) to the data for the model given in table 1 where there is no AVA variation as shown in Figure 2. The AVA response in Figure 4 is seen to be incorrect, with amplitude increasing with angle. This is in accordance with equation (20) predicting amplitudes to increase by a factor $1/\cos^2(\phi)$ where ϕ is the reflection angle.

Figure 5 shows a velocity model with a layer dipping at approximately 18 degrees and a flat reflector below. A synthetic split-spread survey with maximum offset of 5km and a total of 1000 shots was acquired over this model. The first shotpoint was positioned at a horizontal distance of 5km and the last at 15km.

Figure 6 shows an angle gather (left) computed at a horizontal position of 8 km in the model shown in Figure 5 using the shot records described above. Also shown in Figure 5 are the RMS amplitude picks of the two events in the angle gather. The event corresponding to the dipping reflector (Black line) and the event corresponding to the flat reflector (Red line) both show the same amplitude versus angle behavior, as expected.

The effect of ignoring the dip-correction given by equation (25) is shown in Figure 7

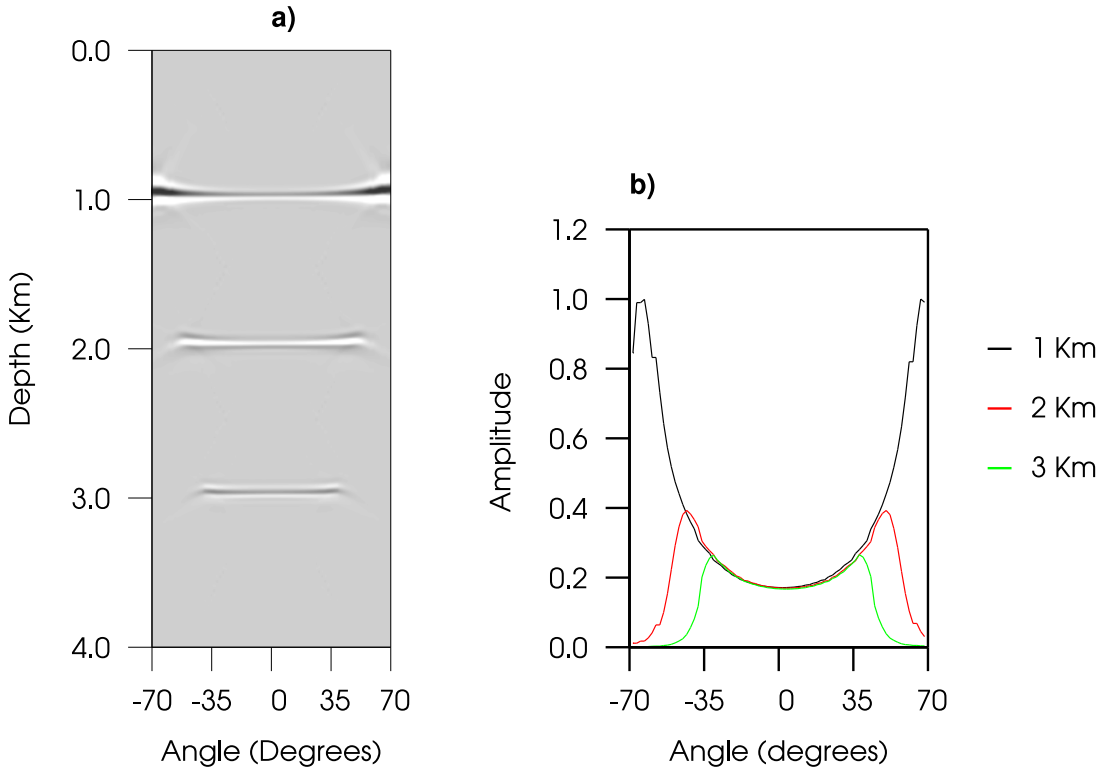

Figure 4: Angle gather computed for the plane layered model given in table 1 using Rickett and Sava (2002) extended imaging condition. b) RMS amplitude picks of the angle gather. The amplitude versus angle is seen to give an incorrect AVA-response, with strongly increasing amplitude with increasing angle.

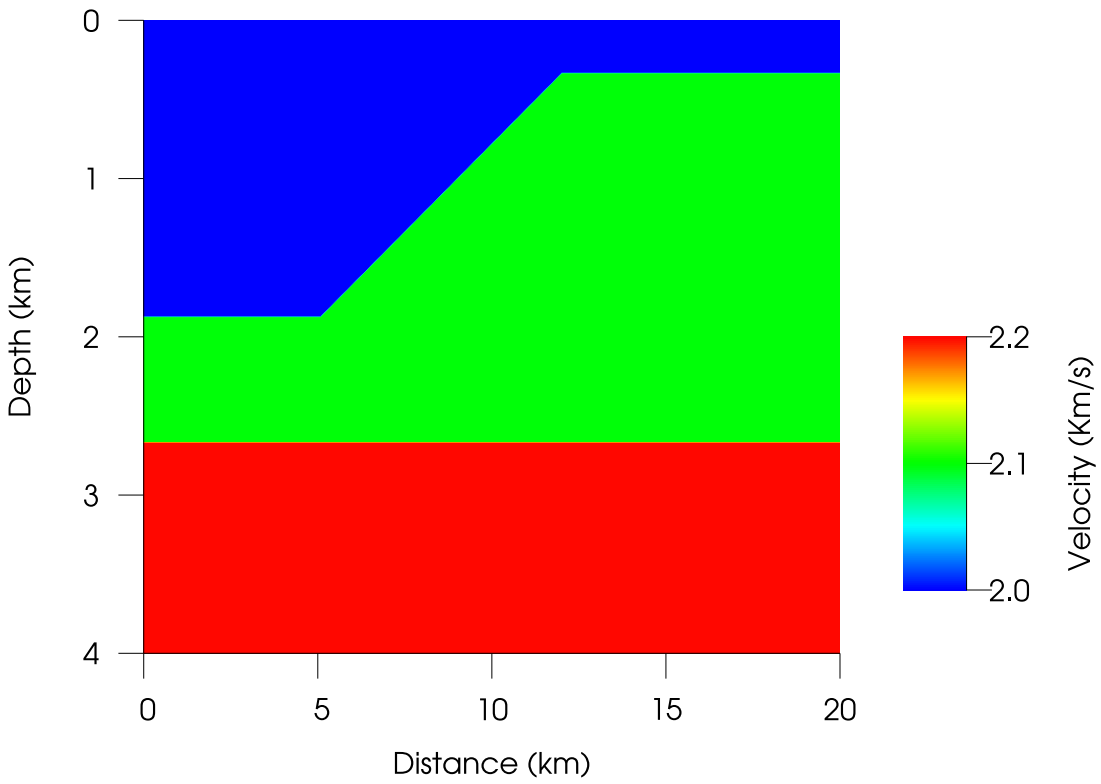

Figure 5: Velocity model with dipping layer.

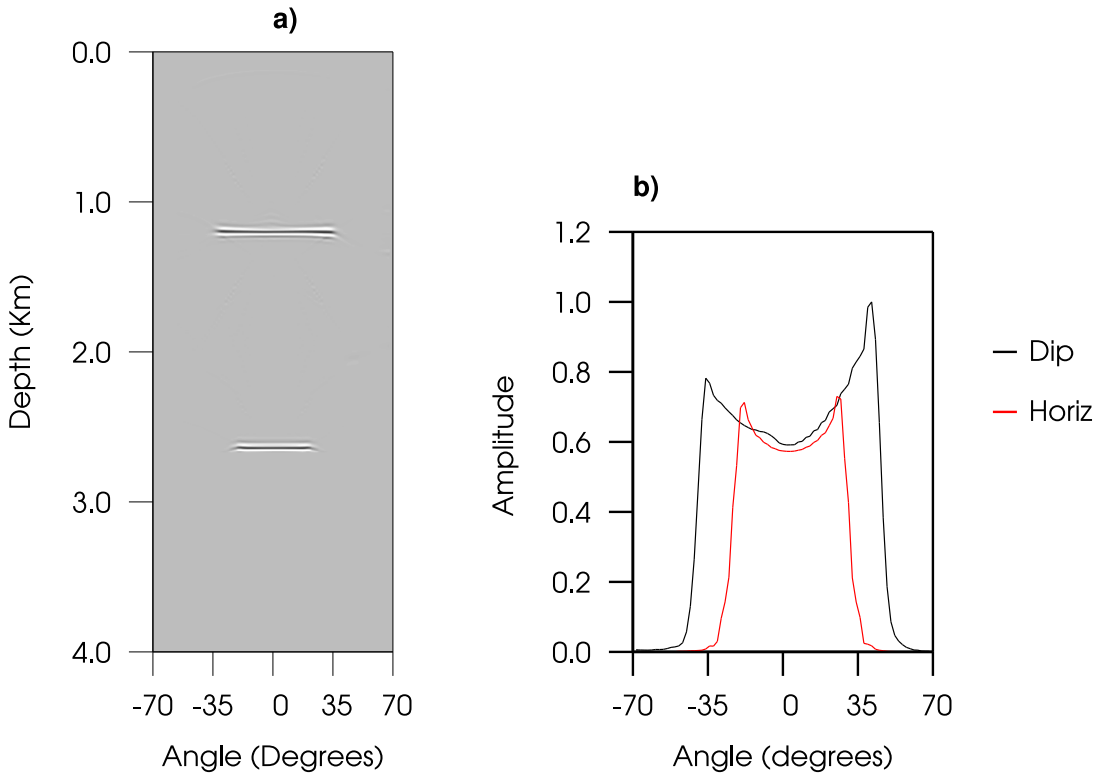

Figure 6: Angle gather computed for the velocity model shown in Figure 5 and b) RMS amplitude picks for the dipping reflector (black line) and the plane reflector (red line).

where the angle gather has been computed using only equation (13), omitting the dip-correction of equation (25). The red line shows the RMS amplitude pick for the horizon-

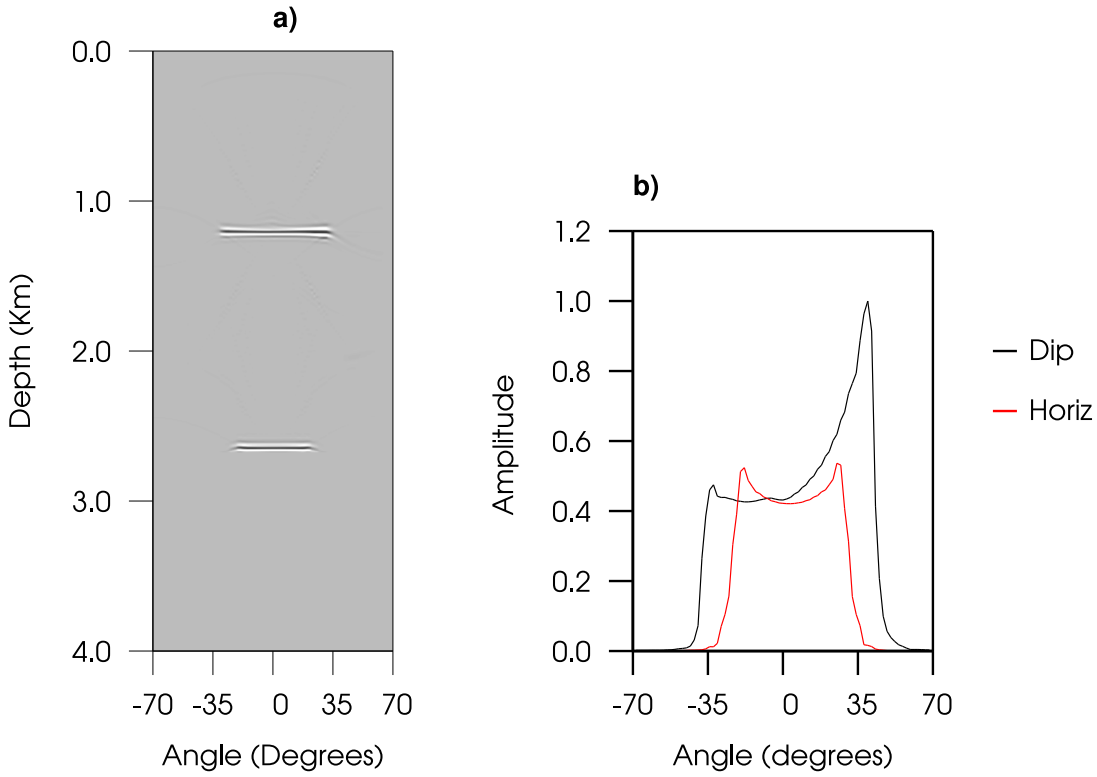

Figure 7: Angle gather computed for the velocity model shown in Figure 5. No dip-correction was applied to the gather. b) RMS amplitude picks for the dipping reflector (black line) and the plane reflector (red line).

tal reflector while the black line shows the corresponding amplitude pick for the dipping reflector.. As can be observed, the amplitude versus angle response is incorrect if the dip-correction is not applied.

Figure 8 shows sections obtained by stacking over all angles, both with (left) and without (middle) the dip-correction.

The difference (right) between these two section is significant, but not large. The angle coverage increases in the up-dip direction due to the acquisition geometry, causing the difference to be larger for the upper part of the reflector. In Figure 9 only a narrow angle range from 23 to 25 degrees have been stacked. The illumination of the dipping reflector is more even in this angle range, the difference is still significant, but not large.

Elastic reservoir model

The imaging condition developed in the preceding sections is valid for an acoustic medium, with acoustic reflection coefficients. In a real data case the reflection coefficients are elastic. However, the model for primary reflections given in equation (1) is approximately valid,

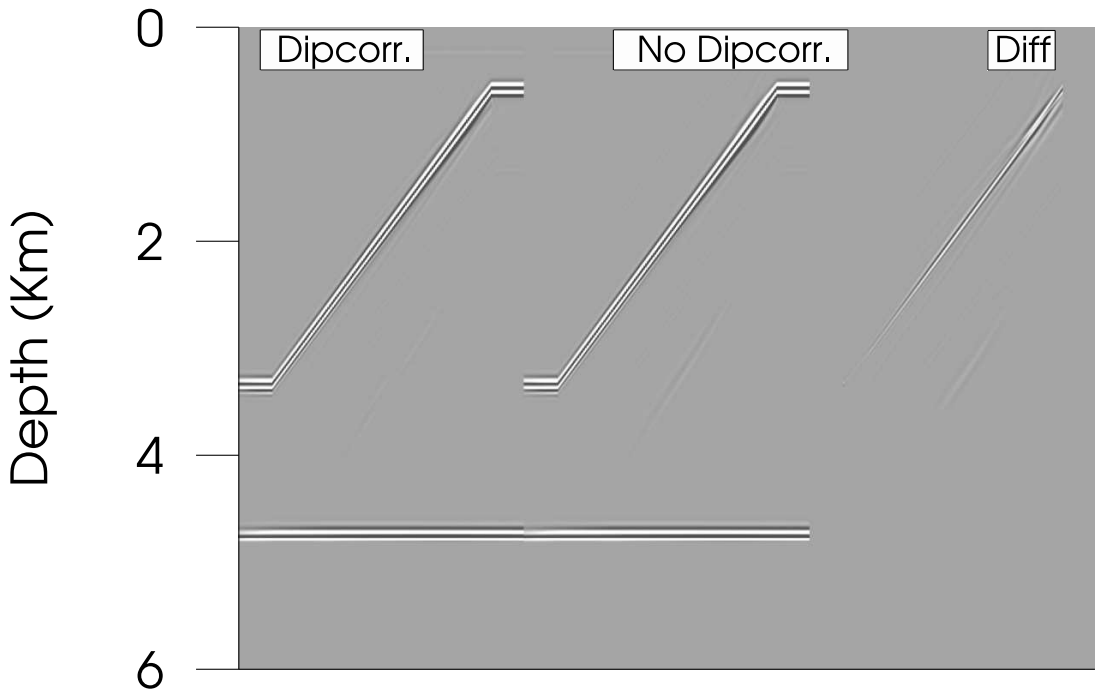

Figure 8: Stack-sections using the data obtained from the model shown in 5. All angles were included in the stacks. The left-hand section were produced from dip corrected angle gathers, while the section in the middle was produced from angle gathers with no dip correction. The section to the right shows the difference.

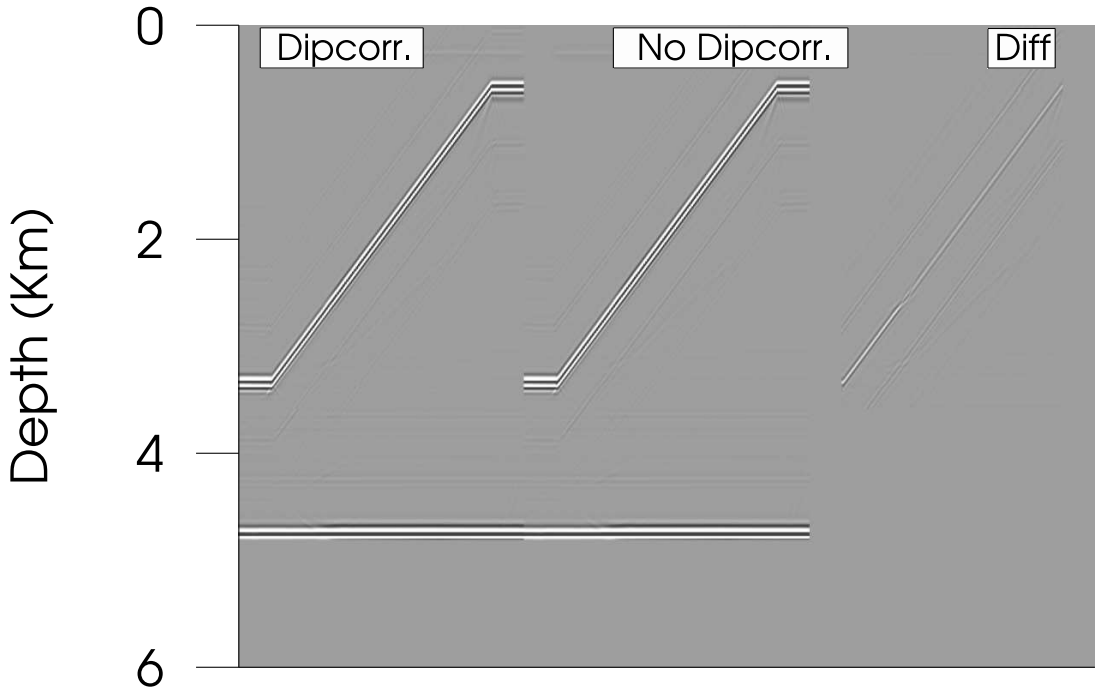

Figure 9: Stack-sections using the data obtained from the model shown in 4. Angles between 23 and 25 degrees were included in the stacks. The left-hand section were produced from dip corrected angle gathers, while the section in the middle was produced from angle gathers with no dip correction. The section to the right shows the difference.

given that the acoustic reflection operator R is replaced with the corresponding elastic reflection operator R_{pp}(Aki and Richards, 1980). This implies that we neglect amplitude loss due to conversions from P-waves to S-waves.

Figure 10 shows a velocity model for from the North Sea. An oil reservoir is located in the middle tilted fault-block at a depth of approximately 2 km. An elastic finite-difference

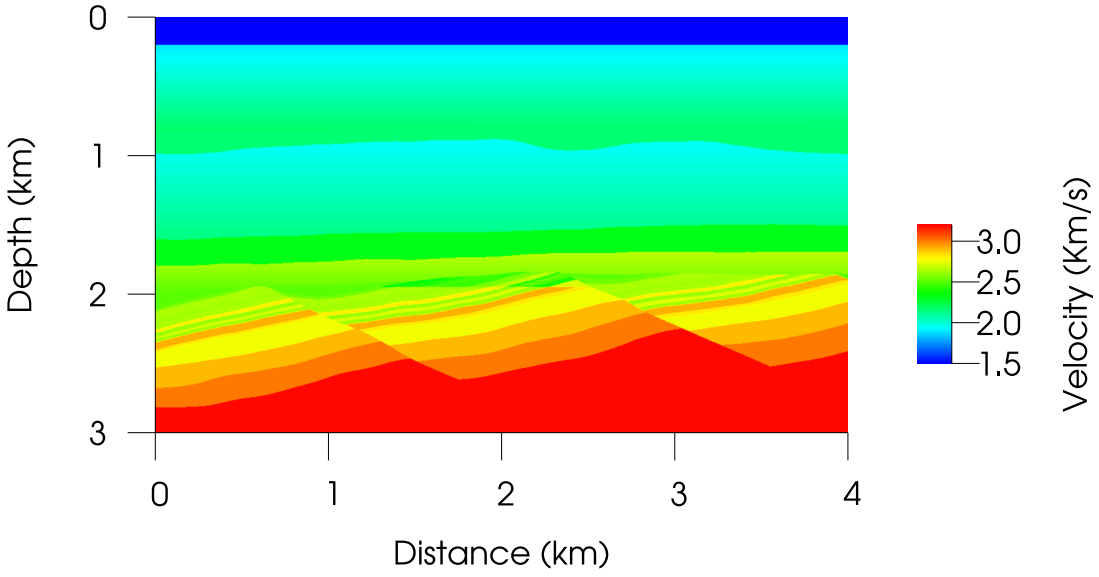

Figure 10: P-wave velocity for the elastic reservoir model

program was used to compute a synthetic marine survey across the velocity model. Angle gathers were computed using the new imaging condition as described in the previous sections, and angle stacks with angles ranging from 8-15 degrees and 25-40 degrees is shown in Figures 11 and 12, respectively. Figure 13 shows an angle gather computed at a horizontal position of 1.7 km, while Figure 14 shows amplitude picks from the gather at the top reservoir reflector located at a depth of 1.850 km and the oil-water contact at a depth of 1.940 km. . Comparison with the reflection coefficients computed from the P-wave, S-wave and density models shows that the new imaging condition reproduces the true AVO-response, except for small angles, where the estimates are incorrect.

The dip-correction given by equation (25) is insignificant for the range of dips for most of the reflectors shown in Figure 14, but will make a difference for the reflections from the steep fault-planes, as shown in Figure 15. The AVA response is significantly different when the dip-correction is applied (circles) and when ignored (crosses).

DISCUSSION

To be able to extract reliable AVA-responses from seismic data, there are several issues involved, two of them being the accuracy of the wavefield extrapolation and the imaging condition itself. Here we deal with the imaging condition and assume that the up- and downgoing wavefields can be computed with sufficient accuracy.

The simple dip correction given by equation (25) is only valid for small contrasts in

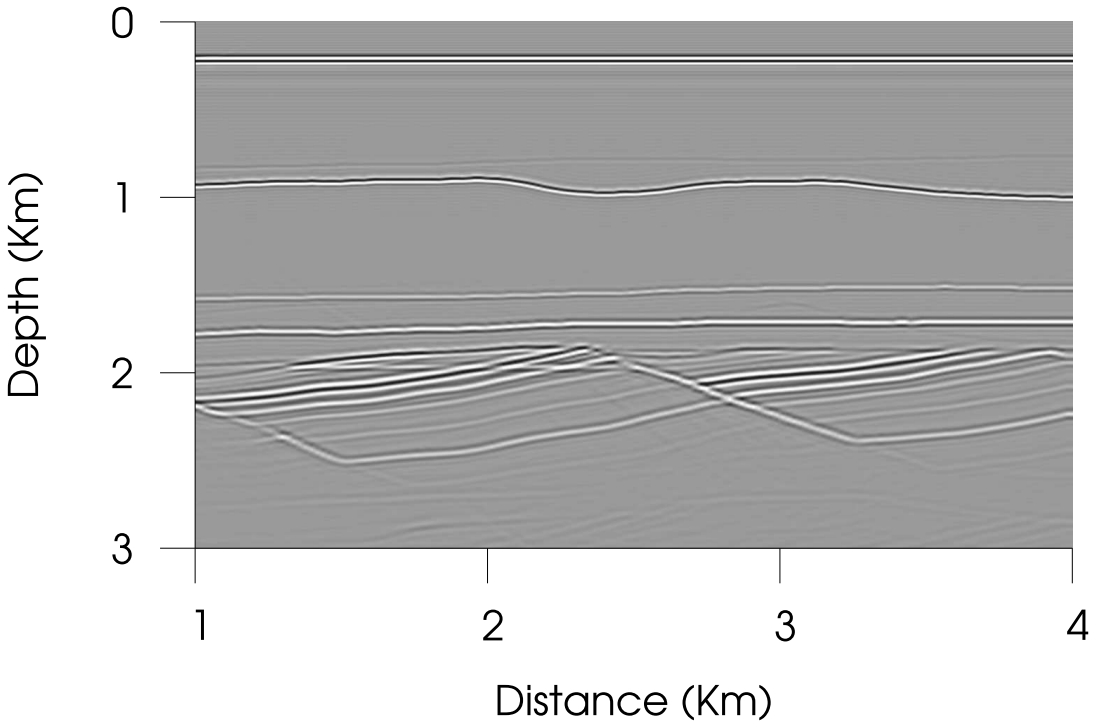

Figure 11: Stack of angle gathers between 8 and 15 degrees of the elastic reservoir model

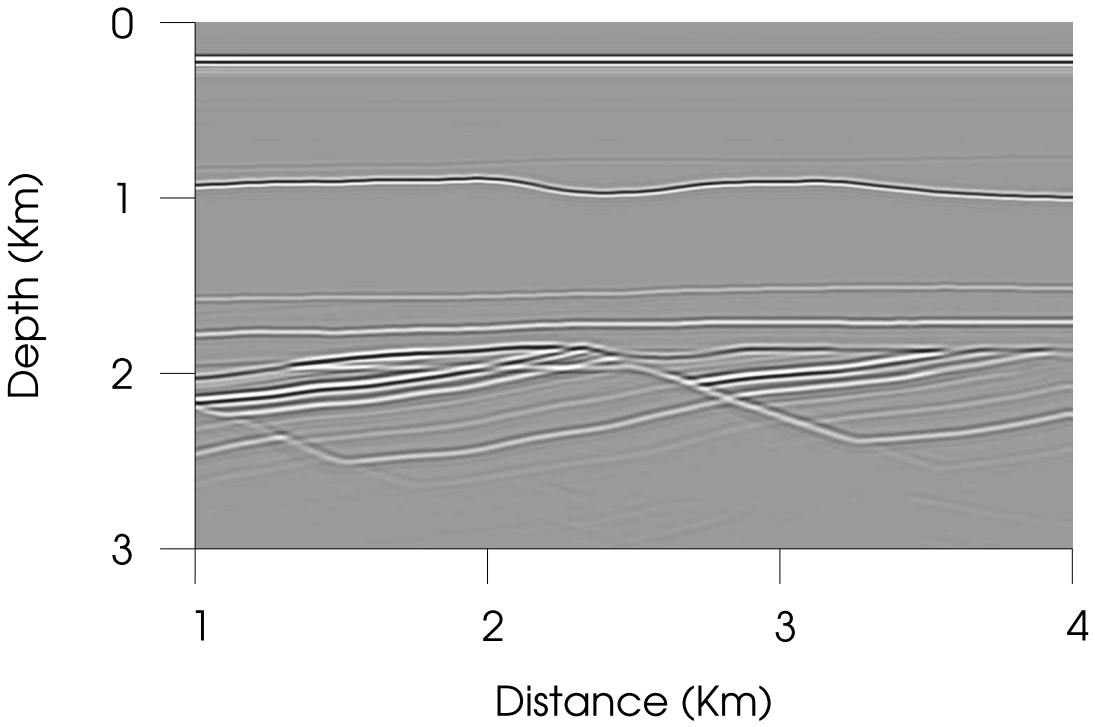

Figure 12: Stack of angle gathers between 24 and 40 degrees of the elastic reservoir model

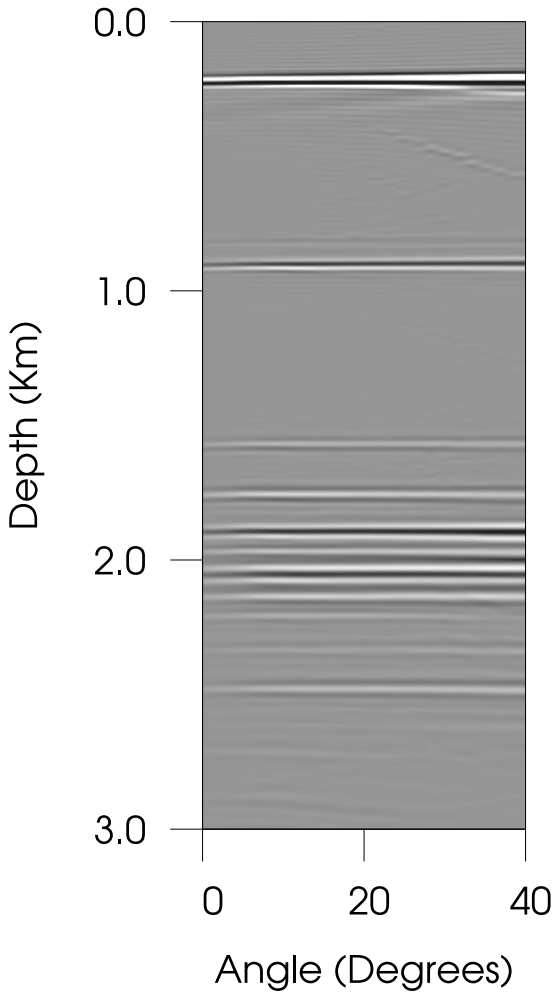

Figure 13: Angle gather at horizontal position of 1700m

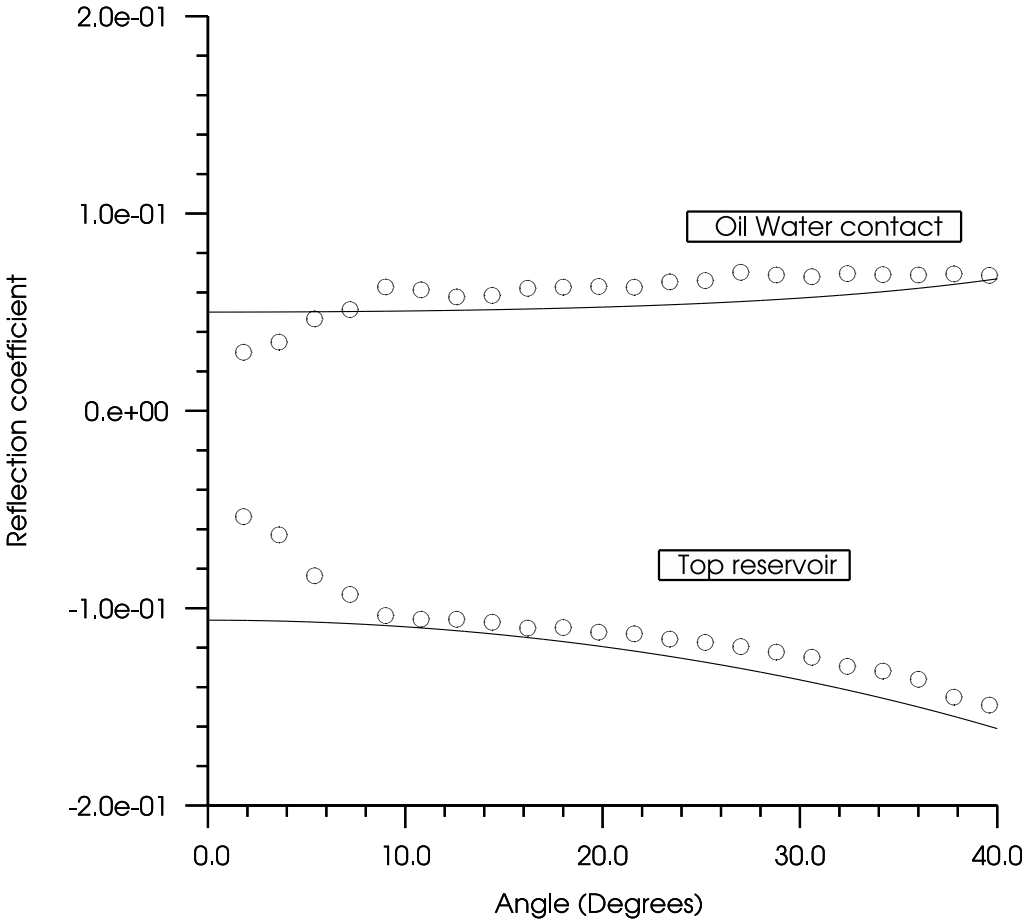

Figure 14: Amplitude picks using the angle gather in figure 13 showing the oil-water contact (above) and top-reservoir (bottom). Circles shows the picks, while the solid line shows exact elastic reflection coefficients

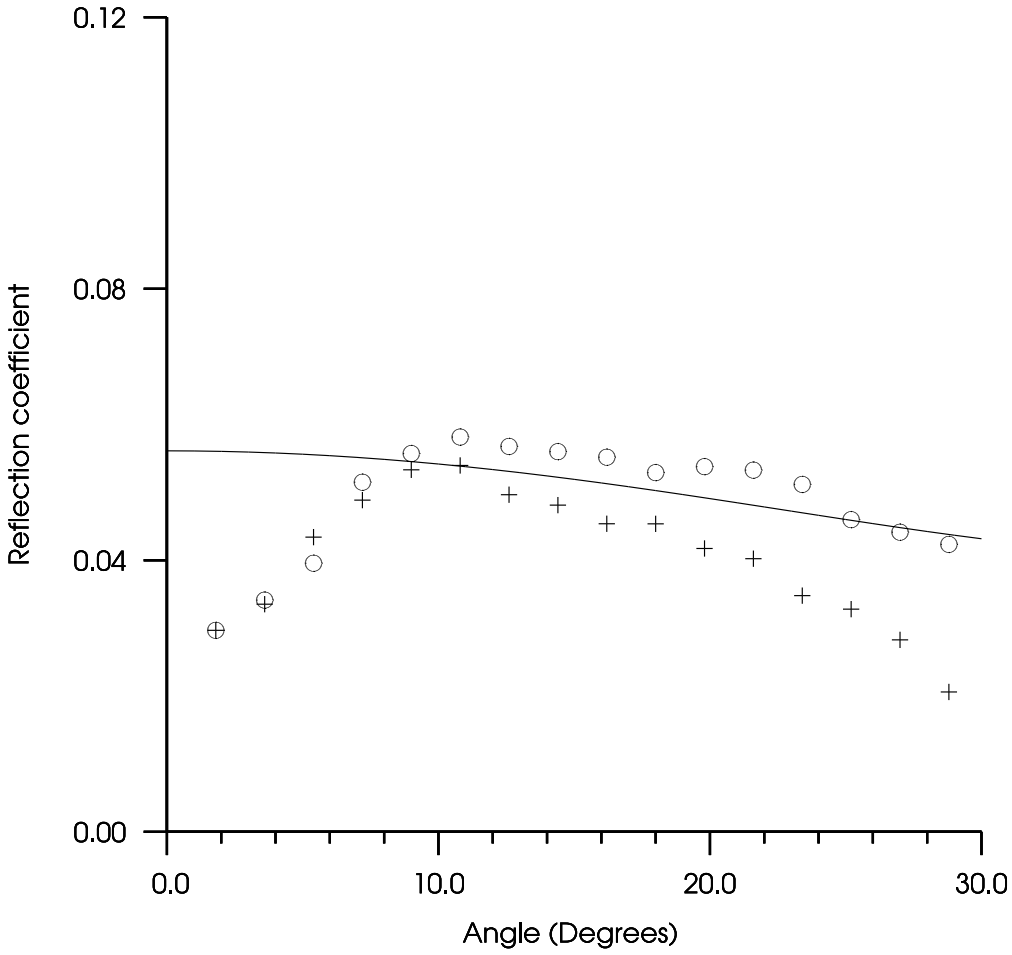

Figure 15: Amplitudes (circles) picked from an angle gather positioned at a distance of 2 km for a reflector at a depth of 2.2 km. The dip of the reflector is 36 degrees. The crosses shows the corresponding picks without applying the dip-correction given by (25).

impedance and for small dip-angles. Also separate information of the local dip is required, and can not be provided by the algorithm itself.

The actual acquisition parameters is a limiting factor for the accuracy of the AVA-response; Figures 14 and 15 demonstrate that a marine single-spread geometry will lead to incorrect estimates of the reflection coefficients for small angles. This can be somewhat improved by careful tapering of the input data, but cannot be completely removed, unless a better split-spread type geometry is used (as in OBC surveys).

CONCLUSIONS

We propose a new source initial condition which stabilizes the classical imaging condition. The new modified imaging condition is of cross-correlation type and avoids instabilities associated with division of wavefields. This results in a cross-correlation wave-equation angle transform which is a direct estimate of the plane-wave reflection coefficient for a plane horizontal reflector. For a dipping plane we propose a simple dip and azimuth correction which gives an approximate estimate of the plane-wave reflection coefficient.

The cross-correlation imaging condition proposed by Claerbout (1971), and extended by Rickett and Sava (2002), can be easily modified to produce correct AVA gathers for locally plane and dipping reflectors. This only involves changing the initial point-source source wavefield to a modified wavefield with a radiation pattern different from a point source, and a post-migration dip-correction.

The results were derived for a scalar wave equation but numerical results show that they can approximately be extended to PP reflections in elastic media.

ACKNOWLEDGEMENTS

We thank the Norwegian Research Council, the sponsors of the ROSE project and Statoil for financial support. Bjørn Ursin has received financial support from VISTA.

APPENDIX A

ONE-WAY WAVE EQUATIONS

We consider an acoustic medium where the density $\rho(z)$ and velocity $c(z)$ is a function of depth only. After Fourier transforming the equations of motion over frequency ω and horizontal wavenumbers $\boldsymbol{k} = k_1, k_2$ one obtains the following matrix equation for the pressure P and the vertical particle velocity V_z (Ursin, 1983)

$$\partial_3 \boldsymbol{b} = i\omega A \boldsymbol{b} \tag{A-1}$$

where the matrix $\boldsymbol{A}$ is

$$\boldsymbol{A} = \begin{bmatrix} 0 & -\rho \\ \frac{1}{\rho}\left(\frac{1}{c^2} - \frac{k_1^2+k_2^2}{\omega^2}\right) & 0 \end{bmatrix}, \tag{A-2}$$

and the vector $\boldsymbol{b}$ is

$$\boldsymbol{b} = \begin{bmatrix} P \\ V_3 \end{bmatrix}. \tag{A-3}$$

The up- and downgoing waves U and D are related to the pressure and vertical particle velocity through the linear transformation

$$\boldsymbol{w} = \begin{bmatrix} U \\ D \end{bmatrix} = \boldsymbol{L}^{-1}\boldsymbol{b}. \tag{A-4}$$

Substituting $\boldsymbol{w}$ for $\boldsymbol{b}$ in equation A-1 leads to the differential equation for $\boldsymbol{w}$

$$\partial_3 \boldsymbol{w} = \left(i\omega\boldsymbol{\Lambda} - \boldsymbol{L}^{-1}\partial_3\boldsymbol{L}\right)\boldsymbol{w}, \tag{A-5}$$

where $\boldsymbol{\Lambda}$ is a diagonal matrix composed of the eigenvalues p_3^u and p_3^d of $\boldsymbol{A}$

$$\boldsymbol{\Lambda} = \boldsymbol{L}^{-1}\boldsymbol{A}\boldsymbol{L} = \begin{bmatrix} -p_3^u & 0 \\ 0 & p_3^d \end{bmatrix}. \tag{A-6}$$

We will also make use of the impedances $Z^d = \rho/p_3^d$ and $Z^u = \rho/p_3^u$.

Pressure normalized wavefields

The eigenvalue matrix of $\boldsymbol{A}$ can be be scaled in different ways. The so-called pressure-normalized scaling corresponds to the following eigenvalue matrix

$$\boldsymbol{L} = \begin{bmatrix} 1 & 1 \\ -1/Z^u & 1/Z^d \end{bmatrix}, \tag{A-7}$$

with inverse

$$\boldsymbol{L}^{-1} = \frac{1}{Z^u + Z^d}\begin{bmatrix} Z^u & -Z^d Z^u \\ Z^d & -Z^d Z^u \end{bmatrix}. \tag{A-8}$$

The differential equation (A-5) becomes

$$\partial_3 \boldsymbol{w} = i\omega\begin{bmatrix} -p_3^u & 0 \\ 0 & p_3^d \end{bmatrix}\boldsymbol{w} + \frac{2}{Z^u + Z^d}\begin{bmatrix} -Z^d r(Z^u) & Z^u r(Z^d) \\ -Z^d r(Z^u) & Z^u r(Z^d) \end{bmatrix}\boldsymbol{w}, \tag{A-9}$$

where $r(Z)$ is given by

$$r(Z) = \frac{1}{2}Z^{-1}\partial_3 Z. \tag{A-10}$$

Neglecting the interaction between up- and downgoing waves, leads to the following simplified differential equation for $\boldsymbol{w}$

$$\partial_3 \boldsymbol{w} = i\omega\begin{bmatrix} -p_3^u & 0 \\ 0 & p_3^d \end{bmatrix}\boldsymbol{w}, \tag{A-11}$$

with solutions

$$U(x_3) = \exp\left(-\int_0^{x_3} ik_3^u(\zeta)d\zeta\right) U_0 \tag{A-12}$$

$$D(x_3) = \exp\left(\int_0^{x_3} ik_3^d(\zeta)d\zeta\right) D_0. \tag{A-13}$$

Here D_0 is the initial downgoing wavefield at the surface for a point source, and U_0 is the measured data at the surface. This solution completely ignores the interaction between the up- and downgoing waves, but a slightly better solution taking the interaction partly into account can be obtained by inserting the approximate solution for the downgoing wavefield given by equation (A-13) back into the right hand side of equation (A-9). By neglecting the diagonal terms and solve for U one gets

$$U(x_3) = \exp\left[-\int_0^{x_3} ik_3^u(\zeta)d\zeta\right] \int_0^{x_3} \exp\left[\int_0^{\zeta} ik_3^d(\zeta')d\zeta'\right] R(\zeta)D(\zeta)d\zeta \tag{A-14}$$

where R is given by

$$R(x_3) = \frac{2Z^u(x_3)}{Z^u(x_3) + Z^d(x_3)} r[Z^d(x_3)]. \tag{A-15}$$

In the simplified case where the reflections are caused by abrupt changes in the material parameters, R can be described by

$$R = R(x_3')\delta(x_3' - x_3), \tag{A-16}$$

and the up-going wave U is then related to the downgoing wave D by

$$U(x_3) = R(x_3)\exp[i(k_3^d - k_3^u)x_3]D(x_3). \tag{A-17}$$

For a horizontal interface $k_3^u = k_3^d$ and we get

$$U(x_3) = R(x_3)D(x_3). \tag{A-18}$$

Flux normalized wavefields

By scaling the eigenvalue matrix of $\boldsymbol{A}$ in the following way

$$\tilde{\boldsymbol{L}} = \frac{1}{\sqrt{2}} \begin{bmatrix} \sqrt{Z^u} & \sqrt{Z^d} \\ -1/\sqrt{Z^u} & 1/\sqrt{Z^d} \end{bmatrix}, \tag{A-19}$$

we get the so-called flux-normalization. The inverse of $\tilde{\boldsymbol{L}}$ is

$$\tilde{\boldsymbol{L}}^{-1} = \frac{1}{\sqrt{2}(Z^u + Z^d)} \begin{bmatrix} \sqrt{Z^u} & -Z^d\sqrt{Z^u} \\ \sqrt{Z^d} & Z^u\sqrt{Z^d} \end{bmatrix}. \tag{A-20}$$

The differential equation (A-5) becomes

$$\partial_3 \boldsymbol{w} = i\omega \begin{bmatrix} -p_3^u & 0 \\ 0 & p_3^d \end{bmatrix} \boldsymbol{w} + \frac{1}{Z^u + Z^d} \begin{bmatrix} (Z^u - Z^d)r(Z^u) & \sqrt{Z^u Z^d}r(Z^d) \\ \sqrt{Z^u Z^d}r(Z^u) & (Z^u - Z^d)r(Z^d) \end{bmatrix} \boldsymbol{w}, \tag{A-21}$$

Neglecting the last term in equation (A-21) leads to

$$\tilde{U}(x_3) = \exp\left(-\int_0^{x_3} ik_3^u(\zeta)d\zeta\right)\tilde{U}_0 \tag{A-22}$$

$$\tilde{D}(x_3) = \exp\left(\int_0^{x_3} ik_3^d(\zeta)d\zeta\right)\tilde{D}_0. \tag{A-23}$$

Inserting equation (A-23) into the right hand side of equation (A-21) and neglecting the diagonal terms gives and expression for the upgoing wavefield:

$$\tilde{U}(x_3) = \exp\left[-\int_0^{x_3} ik_3^u(\zeta)d\zeta\right]\int_0^{x_3}\exp\left[\int_0^{\zeta} ik_3^d(\zeta')d\zeta'\right]\tilde{R}(\zeta)D(\zeta)d\zeta, \tag{A-24}$$

where $\tilde{R}$ is given by

$$\tilde{R}(x_3) = \frac{2\sqrt{Z^u(x_3)Z^d(x_3)}}{Z^u(x_3)+Z^d(x_3)}r[Z^d(x_3)]. \tag{A-25}$$

In the simplified case where the reflections are caused by abrupt changes in the material parameters the up-going wave $\tilde{U}$ is then related to the downgoing wave $\tilde{D}$ by

$$\tilde{U}(x_3) = \tilde{R}(x_3)\exp[i(k_3^d - k_3^u)x_3]\tilde{D}(x_3). \tag{A-26}$$

For a plane horizontal interface $k_3^u = k_3^d$ and we then get

$$\tilde{U}(x_3) = \tilde{R}(x_3)\tilde{D}(x_3). \tag{A-27}$$

APPENDIX B

AMPLITUDE CORRECTION FOR DIPPING LAYER

We consider an interface with dip-angle α relative to the vertical direction and azimuth angle θ in the direction of maximum dip.

A downgoing wave reflected at the interface has an incoming angle equal to ϕ, measured relative to the surface normal of the interface. Due to Snell's law, the outgoing angle is also equal to ϕ. By simple geometry, the incoming and outgoing angles θ_u and θ_d, measured relative to the vertical direction is given by

$$\begin{aligned}\theta_u &= \phi + \alpha,\\ \theta_d &= \phi - \alpha.\end{aligned} \tag{B-1}$$

The vertical slowness p_3 is given by

$$\begin{aligned}p_3^d &= \cos(\phi-\alpha)/c,\\ p_3^u &= \cos(\phi+\alpha)/c,\end{aligned} \tag{B-2}$$

which gives the impedances Z^d and Z^u

$$\begin{aligned}Z^d &= \rho c/\cos(\phi-\alpha)\\ Z^u &= \rho c/\cos(\phi+\alpha).\end{aligned} \tag{B-3}$$

From equation (A-15) we have for the reflection coefficient for pressure-normalized waves

$$R(x_3) = \frac{2\cos(\phi+\alpha)}{\cos(\phi-\alpha)+\cos(\phi+\alpha)} r(x_3), \tag{B-4}$$

For the flux-normalized case we have similarly from equation (A-25)

$$\tilde{R}(x_3) = \frac{2\sqrt{\cos(\phi+\alpha)\cos(\phi-\alpha)}}{\cos(\phi-\alpha)+\cos(\phi+\alpha)} r(x_3). \tag{B-5}$$

From equations (B-4) and (B-5) it is clear that the plane-wave reflection coefficient for a plane layer can easily be obtained from equations (B-4) and (B-5).

REFERENCES

Aki, K., and P. G. Richards, 1980, Quantitative seismology: W.H. Freeman and Co.

Bleistein, N., 1987, On the imaging of reflectors in the earth: Geophysics, **52**, 931–942.

Cazzola, L., M. Arienti, E. Bonomi, and G. Cardone, 2002, Amplitude-preserving monte carlo 3D prestack migration: EAGE, Expanded Abstracts, B009.

Claerbout, J. F., 1971, Toward a unified theory of reflector mapping: Geophysics, **36**, 467–481.

de Bruin, C., C. Wapenaar, and A. Berkhout, 1990, Angle-dependent reflectivity by means of prestack migration: Geophysics, **55**, 1223–1234.

Deng, F., and G. A. McMechan, 2007, True-amplitude prestack depth migration: Geophysics, **72**, S155–S166.

Holberg, O., 1988, Towards optimum one-way wave propagation: Geophysical Prospecting, **36**, 99–114.

Rickett, J., and P. C. Sava, 2002, Offset and angle-domain common image-point gathers for shot-profile migration: Geophysics, **67**, 883–889.

Schleicher, J., J. C. Costa, and A. Novais, 2008, A comparison of imaging conditions for wave-equation shot-profile migration: Geophysics, **73**, S219–S227.

Schleicher, J., M. Tygel, and P. Hubral, 1993, 3-D true-amplitude finite-offset migration: Geophysics, **58**, 1112–1126.

Tygel, M., J. Schleicher, P. Hubral, and C. Hanitzsch, 1993, Multiple weights in diffraction stack migration: SEG Technical Program Expanded Abstracts, **12**, 1040–1043.

Ursin, B., 1983, Review of elastic and electromagnetic wave propagation in layered media: Geophysics, **48**, 1063–1081.

———, 2004, Parameter inversion and angle migration in anisotropic elastic media: Geophysics, **69**, 1125–1142.

Ursin, B., . Pedersen, and B. Arntsen, 2012, Flux.normalized wavefield decomposition and migration of seismic data: Geophysics, **Accepted for publication**.

Valenciano, A. A., and B. Biondi, 2003, 2D deconvolution imaging condition for shot-profile migration: SEG, Expanded Abstracts, **22**, 1059–1062.

Zhang, Y., and J. Sun, 2008, Practical issues of reverse time migration: true-amplitude gathers, noise removal and harmonic-source encoding: Extended Abstracts 70th EAGE Conference and Exhibition, Rome, taly.

Zhang, Y., G. Zhang, and N. Bleistein, 2005, Theory of true-amplitude one-way wave equations and true-amplitude common-shot migration: Geophysics, **70**, E1–E10.